UNIVERSITY OF BRISTOL

University of Bristol - Explore Bristol Research
General rights

Presynaptic Boutons That Contain Mitochondria Are More Stable

Robert M. Lees[†], James D. Johnson[†] and Michael C. Ashby*

School of Physiology, Pharmacology, and Neuroscience, Faculty of Biomedical Sciences, University of Bristol, Bristol, United Kingdom

The addition and removal of presynaptic terminals reconfigures neuronal circuits of the mammalian neocortex, but little is known about how this presynaptic structural plasticity is controlled. Since mitochondria can regulate presynaptic function, we investigated whether the presence of axonal mitochondria relates to the structural plasticity of presynaptic boutons in mouse neocortex. We found that the overall density of axonal mitochondria did not appear to influence the loss and gain of boutons. However, positioning of mitochondria at individual presynaptic sites did relate to increased stability of those boutons. In line with this, synaptic localization of mitochondria increased as boutons aged and showed differing patterns of localization at *en passant* and *terminaux* boutons. These results suggest that mitochondria accumulate locally at boutons over time to increase bouton stability.

Keywords: presynaptic bouton, synaptic plasticity, *in vivo* 2-photon imaging, mitochondria, neocortex, synapse turnover

INTRODUCTION

Individual cortical presynaptic terminals can be added and removed on axonal branches on a timescale ranging from days to years (De Paola et al., 2006; Grillo et al., 2013; Mostany et al., 2013; Qiao et al., 2015). Alterations in this presynaptic turnover are related to learning (Holtmaat and Caroni, 2016; Johnson et al., 2016; Ash et al., 2018) and disease (Jackson et al., 2017), showing their importance for the plasticity of neural circuits. However, little is known about cellular control of bouton structural plasticity, although it has been suggested that mitochondria may play a role (Smit-Rigter et al., 2016).

Mitochondria and synaptic efficacy are strongly linked. Ultrastructural features of efficacy (e.g., postsynaptic density size or number of docked vesicles) are positively correlated to presynaptic mitochondria (Kasthuri et al., 2015; Smith et al., 2016; Cserép et al., 2018), mitochondrially-derived ATP is required to sustain neurotransmission during elevated levels of stimulation (Hall et al., 2012; Rangaraju et al., 2014; Sobieski et al., 2017) and mitochondria modulate presynaptic release by sequestering cytosolic calcium or altering ATP concentrations (Sun et al., 2013; Kwon et al., 2016; Vaccaro et al., 2017; Lewis et al., 2018). However, mitochondria only localize to a subpopulation of boutons (Chang et al., 2006; Kang et al., 2008; Obashi and Okabe, 2013; Smit-Rigter et al., 2016; Vaccaro et al., 2017) and very little is known about whether the spatial distribution of mitochondria relative to presynaptic sites is related to bouton formation, longevity or removal (Smit-Rigter et al., 2016). To address this, we have used chronic, *in vivo* two-photon (2P) imaging to investigate the relationship between mitochondrial localization in axons and the structural plasticity of presynaptic boutons.

MATERIALS AND METHODS

Item	Supplier	Description	Code
AAV2/1-hSyn-EGFP-P2A-MTS-TagRFP-WPRE at 1–2×10^{13} GC ml^{-1}	Eli Lilly	Custom viral vector	
Cortex buffer		125 mM NaCl, 5 mM KCl, 10 mM Glucose, 10 mM HEPES, 2 mM CaCl$_2$, 2 mM MgSO$_4$ in dH$_2$O, pH 7.4	
Glass microcapillary	Harvard apparatus	Borosilicate, thin wall, without filament, Clark capillary glass	300035
Skull screw	Bilaney	0–80 UNF thread × 1/16 inch length	
Vetbond	Vet tech solutions	Surgical adhesive	IN004
Coverslip (cranial window)	Harvard Apparatus	CS-5R Coverslips, 0.15 mm (0.006 in), 5 mm diameter, pack of 100	640700
Stainless steel head bar		Custom-made, 10 × 3 × 1 mm with 2 × M2 holes centered 2 mm from each end	
Bone cement	DePuy	With gentamicin	
Hydrogel solution kit	Logos biosystems		C1310X
Electrophoretic tissue clearing solution	Logos biosystems		C13001
Mounting solution (cleared brain)	Logos biosystems	X-CLARITY mounting solution	C13101
Fluoromount-Gw/DAPI	Thermo Fisher Scientific		00-4959-52

Equipment

Item	Supplier	Description
Two-photon microscopy (*in vivo imaging*)	Scientifica	Custom-built with filter cube carousel and epifluorescence capabilities
Ti-Sapphire laser	Spectra-Physics	MaiTai Ti-Sapphire tuneable laser (680–1, 040 nm)
60× water-immersion objective	Olympus	For *in vivo* 2P imaging, 1.1 NA
X-CLARITY tissue clearing system	Logos Biosystems	
Two-photon microscopy (cleared brain imaging)	Leica	Leica SP8 AOBS laser-scanning microscope w/Leica DM6000 upright epifluorescence microscope
Ti-Sapphire laser	Spectra-Physics	MaiTai DeepSee Ti-Sapphire tuneable laser (680–1,300 nm)

Software

Software	Developer	Version	Description
ScanImage	Vidrio technologies	5.1	Two-photon microscope control
Micromanager	Open imaging	1.4	Camera control
ImageJ (FIJI package)	ImageJ Development Team	1.51a (2.0.0-rc-43)	Image processing and analysis
MATLAB	MathWorks	R2016a	Data processing and analysis
Prism	GraphPad	7	Graph making and basic statistical testing
G*Power	Universität Düsseldorf		Statistical power calculations
SPSS statistics	IBM	24	Statistical testing

Animal Husbandry

All procedures involving animals adhered to the Animals (Scientific Procedures) Act 1986 and Amendment Regulations 2012 as outlined in UK law and approved by the University of Bristol Animal Welfare and Ethics Review Board.

Adult (2.5 months old) C57Bl/6 male mice were used for all experiments, living on a 12-h light-dark cycle. Animals were housed individually to avoid loss of the cranial window implant due to fighting. Large (∼30 × 50 × 25 cm) cages were used and extra enrichment was provided for each cage, consisting of tunnels, shelters, wheels and foraging food to increase experience-dependent turnover of presynaptic terminals (Briones et al., 2004; Nithianantharajah et al., 2004; Landers et al., 2011).

Viral DNA Construct

The virus used for intracranial injection was a custom-made adeno-associated virus (AAV) of serotype 2/1 expressing a bi-cistronic vector (AAV2/1-hSYN-EGFP-P2A-MTS-TagRFP).

The human synapsin promoter (hSYN) was used to limit expression to neuronal cells. Cytosolic enhanced green fluorescent protein (EGFP) was separated by a P2A peptide from mitochondrially-targeted tagRFP (red fluorescent protein, fused to amino acids 1–29 of Cox8a subunit of cytochrome oxidase), which localized to the inner mitochondrial membrane. The P2A peptide is a self-cleaving peptide of the 2A family from porcine teschovirus, which has a high cleaving efficiency (Kim et al., 2011). Additionally, Woodchuck Hepatitis Virus Posttranscriptional Regulatory Element was used to increase protein expression (Zufferey et al., 1999). The viral titer used for injections was in the range of 1–2×10^{13} particles ml^{-1} in cortex buffer (125 mM NaCl, 5 mM KCl, 10 mM Glucose, 10 mM HEPES, 2 mM CaCl$_2$, 2 mM MgSO$_4$ in dH$_2$O, pH 7.4).

Surgery

To reduce stress, animals were allowed at least 1 week to acclimatize to unfamiliar environments after relocation before

the commencement of procedures. Intraperitoneal injections of Rimadyl (analgesic, 4 mg ml^{-1} kg^{-1}) and dexamethasone (anti-inflammatory, 0.5 mg ml^{-1} kg^{-1}) were given pre-operatively to reduce pain and inflammation. Aseptic technique was used to limit the possibility of infection, guidelines were followed as outlined by the Laboratory Animal Science Association[1]. The protocol described in Holtmaat et al. (2009) was followed for cranial window implantation, which is briefly described below with amendments.

Animals were anesthetized using gaseous isoflurane at 3–4% for induction and 1–2% to sustain anesthesia throughout surgery, carried by O$_2$. The top of the head was shaved and placed in a stereotaxic frame, and the scalp and periosteum were removed. The skull bone was kept moist throughout surgery with cortex buffer.

The intracranial viral injection site was measured +0.7 mm lateral (always to the right) and +1.0 mm anterior from Bregma, as these coordinates correspond to the primary/secondary motor cortex (Lein et al., 2007; Petreanu et al., 2012). A small (∼0.5 mm diameter) burr hole was made in the skull using a high-speed motorized hand drill. For viral injections, a glass capillary tube was pulled into a micropipette with a long, pointed tip and beveled on a whetstone to sharpen it further. The virus was injected intracranially using a Hamilton syringe and motorized pump at a rate of 100 nl/min. A volume of 300 nl was injected at depths of 300 μm (first) and 700 μm (second) from the pial surface to spread it across all cortical layers. The virus was allowed to spread for 3 min before moving the micropipette.

After viral injection, a screw (0–80 UNF thread, 1/16 inch length) was implanted in the left parietal skull bone to anchor the cranial window implant to the skull. Subsequently, a thin layer of VetBond^{TM} glue was spread across the skull, to the skin edges, avoiding the right parietal skull bone where the cranial window was to be implanted. A 3–4 mm diameter craniectomy was made using a motorized hand drill centered on +2.5 mm lateral and −1.8 mm anterior of Bregma. A 5 mm circular glass coverslip was then secured over the craniectomy on top of a small volume of cortex buffer using VetBond^{TM} glue.

Quick-drying bone cement (with gentamycin, DePuy) was used to apply a 1–2 mm thick layer of cement over the layer of VetBond^{TM} glue. Cement was spread just over the edge of the coverslip as well as up to the edges of the skin incision. A stainless-steel bar (10 × 3 × 1 mm; used for securing the head during *in vivo* imaging) was placed over the left hemisphere as close to the cranial window as possible while leaving enough space for microscope objective access.

Animals were left for ∼24 days before imaging to allow for any inflammation to clear under the window and to allow viral expression.

In vivo Imaging

For *in vivo* imaging, a customized Scientifica upright 2P microscope was used along with a motorized stage to aid precise movement in coordinate space for relocation of regions of

[1]http://www.lasa.co.uk/wp-content/uploads/2017/04/Aseptic-surgery-final.pdf

interest (ROIs). Epifluorescence was used for low-resolution mapping of expression across the window to guide 2P imaging. Two MaiTai Ti-Sapphire tuneable lasers (tuneable from 680 to 1,040 nm, Spectra-Physics) were used and attenuation of laser power was controlled through either a Pockel's cell or half-wave plate. 2P excitation wavelengths for imaging were typically 920 nm (EGFP) and 1,040 nm (TagRFP). Laser lines were combined using a polarising beamsplitter cube in reverse, and combined power never exceeded 60 mW at the back focal plane of the objective. The acquisition was controlled by ScanImage software (Pologruto et al., 2003, version 5.1) and Micromanager software (Edelstein et al., 2014, version 1.4). Objective lenses used: 4× air 0.15 NA, 10× water-immersion 0.6 NA and 60× water-immersion 1.1 NA. Emission filter sets used for PMTs were BP 620/60 nm for TagRFP and BP 525/50 nm for EGFP. The stage was fitted with a micromanipulator for precise head fixation and rotation in every repeated imaging session using the implanted steel bar on the animal's head, increasing ROI relocation efficiency. During *in vivo* imaging, mice were anesthetized by gaseous isoflurane anesthetic (1–2% carried by O$_2$) and breathing was monitored to judge depth of anesthesia. Breathing was kept in the range of 80–100 beats per minute by eye.

For each mouse, a large blood vessel bifurcation was chosen using reflected light and set as the origin for recording coordinates of ROIs. 2P imaging was used to locate ROIs based on the following criteria: sparse labeling, to reduce background and contamination from crossing axons; distinctive axonal structures, for easy relocation; distance from other ROIs, to increase the diversity of sampling.

Z-stacks of 20–50 μm were acquired at each ROI with a step size of 1 μm (60×, 1.1 NA objective). Images were acquired with 3× frame averaging, 1 μs pixel dwell time at 1,024 × 1,024 pixels and a field of view of 76 × 76 μm, resulting in a final pixel size of 74 nm. Signal was matched between sessions by adjusting laser power because of differences in window quality between imaging sessions, which altered the signal-to-noise ratio. Up to seven ROIs were chosen per animal and each imaging session was kept between 1 and 2 h.

Axons were tracked for up to 35 days after the initial session, for a total of nine sessions (ethical limit) or until the cranial window was no longer optically clear due to bone regrowth or dural thickening. A small proportion of ROIs were first tracked at days one and two, rather than day zero of the imaging paradigm. Most ROIs and animals were tracked for the entire imaging time series.

Histology

Following the end of an imaging paradigm, mice were administered a dose of 70–100 μl of Euthatal (200 mg/ml sodium pentobarbital) intraperitoneally to achieve terminal anesthesia. When the animal was deeply anesthetized, exsanguination was performed, and the animal was transcardially perfused with 5–10 ml of 0.01 M PBS. This was followed by an infusion of 20–30 ml of 4% paraformaldehyde (PFA) in 0.01 M PBS. The brain was then dissected out and post-fixed in 4% PFA in 0.01 M PBS at 4°C.

Tissue Clearing

Tissue clearing was carried out by following the protocol described in Lee et al. (2016), which is briefly outlined below. The brain was post-fixed for 24 h in 4% PFA followed by overnight incubation in hydrogel solution (4% w/v acrylamide without bis-acrylamide, 1% w/v VA-044 initiator in 0.01 M PBS) at 4°C. Oxygen was removed from the solution by degasification using pure nitrogen bubbling through the solution (providing some agitation). Polymerization of the hydrogel was carried out at 37°C in a water bath for ~3 h. The brain was then mounted inside the X-CLARITY electrophoresis chamber (Logos Biosystems) in electrophoretic tissue clearing solution (4% SDS and 200 mM boric acid). The X-CLARITY machine was used according to the manufacturer's instructions.

Tissue Sectioning

Histological sectioning was achieved using either a vibratome or freezing microtome. For vibratome sectioning, brains were embedded in 2% agarose (in distilled H_2O), trimmed to the region of interest and series of 50 μm-thick sections were cut in 0.01 M PBS on a vibratome. For freezing microtomy, brains were incubated in a 30% sucrose solution (w/v) for up to 1 week. The brains were then sectioned in optimal cutting temperature (OCT) solution. The sections were directly mounted on glass microscope slides with No. 1.5 coverslips using Fluoromount-G containing DAPI nuclear stain.

Imaging of Tissue Sections

Imaging of whole tissue sections was carried out on a widefield microscope (Leica DMI6000) with a mercury lamp and CCD camera (Leica DFC365FX monochrome) using Leica LAS X software. Filter sets were assigned for the following fluorophores: DAPI (Ex. 350/50 nm, 400 nm dichroic mirror, Em. BP 460/50 nm), EGFP (Ex.: 480/40 nm, 505 nm dichroic mirror, Em. BP 527/30 nm), TagRFP (Ex. 620/60,660 nm dichroic mirror, Em. BP 700/38). Objective lenses used: 5× dry 0.15 numerical aperture (NA) and 20× dry 0.4 NA. Brightfield and DAPI signal of coronal or sagittal tissue sections were compared to the Paxinos Mouse Brain Atlas (Franklin and Paxinos, 2008) or Allen Mouse Brain Atlas (Lein et al., 2007) as a reference to confirm the positions of viral injections and window sites.

Imaging of Cleared Tissue

The cleared brain was immersed in a small volume (5–10 ml) of mounting medium (X-CLARITY mounting solution) inside a 50 ml Falcon tube for at least 2 h before mounting. It was then placed in the center of a circular wall of Blu-tac inside the lid of a 35 mm dish to create a water-tight well. The well was filled partially with fresh X-CLARITY mounting medium and the chamber was sealed on top with a 35 mm coverslip pressed into the Blu-tac. The chamber was filled from a small inlet in the Blu-tac using a 200 μl pipette and the inlet was sealed by squeezing the Blu-tac back together.

Cleared tissue was imaged using a Leica SP8 AOBS confocal laser scanning microscope attached to a Leica DM6000 upright epifluorescence microscope with a Ti-Sapphire laser (MaiTai DeepSee; tuneable from 680 to 1,300 nm) and a fixed-wavelength 1,040 nm laser. Two-hybrid GaAsP detectors were used with a

BP 525/50 nm filter for EGFP and BP 630/75 nm for TagRFP. Objectives lenses used: 10× water-immersion 0.3 NA and 25× water-immersion 0.95 NA. Large z-stack mosaic images (5 μm steps for ~1 mm) were acquired using the tilescan function in Leica LAS X software. The laser intensity was attenuated at shallower imaging depths to maintain the signal-to-noise ratio. The images were then resliced to obtain the correct viewing angle.

Image Processing

In vivo images were processed using the FIJI package for ImageJ (Schindelin et al., 2012, version 2.0.0-rc-43/1.51a) and a custom ImageJ macro. The macro allowed for automated processing of images for each ROI, carrying out the following functions: (1) alignment of the EGFP signal within a single z-stack to correct drift and application of the transformation to the TagRFP channel using the MultiStackReg registration plugin; (2) matching of z-stack sizes between time-points by addition of blank slices; (3) alignment of z-stacks between time-points in the x- and y-axes using maximum z-projections and the MultiStackReg plugin; and (4) alignment of z-stacks in the z-axis using an edited version of the Correct 3D Drift plugin to only include the z-axis transformation. This resulted in a 5-dimensional (5D—XYZCT) stack of each ROI aligned to within 5 μm in x, y and z for both channels across all timepoints. For presentation in figures only, images were cropped and had brightness and contrast adjusted and a median filter (74 nm kernel) applied.

Data Quantification

Axonal segments were manually traced using the segmented line tool with spline as part of a custom ImageJ macro script. After tracing at each time point, a minimum volume that encompassed the axon across all the timepoints was cropped from the original 5D stack. Between 1 and 12 axonal segments were chosen from each ROI. Factors used to choose axonal segments were: good signal-to-noise (subjective measure by the analyst), few crossing axons and existence in all time-points.

Identification and indexing of presynaptic terminals and mitochondria were carried out manually on each cropped axonal segment using a custom ImageJ macro script and the multi-point tool. A gaussian blur (sigma = 2 pixels, 154 nm) was used to smooth the signal and presynaptic terminals were scored subjectively, using the local intensity profile as a guide (further information below). The position of each object (bouton or mitochondrion) was estimated from a point placed by the analyst.

Boutons were tracked across imaging sessions from the first timepoint they were identified. Boutons in separate timepoints were linked if they were in the same place relative to fiducial markers, including any crossing axons, kinked structure or other persistent boutons. Any bouton that was lost from the field of view for one timepoint (through a shift in alignment in the x- or y-axes) was excluded entirely. All boutons were scored blind to the mitochondrial signal.

En passant boutons (EPBs) were larger in volume than the axon backbone and therefore had higher intensity relative to the backbone due to increased numbers of fluorescent molecules (cytosolic EGFP). An EPB had to have contiguous pixels in

the x-, y- and z-axes to ensure it was not the result of noise. The intensity profile of an EPB needed to include sharp edges (relatively steep curve either side of the peak) to exclude gentle changes in the axonal thickness. If the peak of an EPB was twice that of the local axon backbone (1.5 μm either side of the bouton) at any time point, the bouton was scored as being present. A bouton was scored as lost if it was below 1.3 times the local axon backbone. These criteria have been shown to be faithful indicators of synapse presence in correlative light and electron microscopy studies (Grillo et al., 2013; Song et al., 2016).

Terminaux boutons were scored as unilateral protrusions from the axon backbone with a bulbous appearance and sometimes consisted of a resolved thin neck that extended for less than 5 μm. Those extending for longer than 5 μm were considered to be axonal branches (Grillo et al., 2013).

A small proportion of boutons changed bouton type (*en passant* or *terminaux*) over the time series and so those boutons were classified based on their predominant type.

Mitochondria were identified as discrete objects that were 2× the global median background signal, with contiguous pixels in the x-, y- and z-axes and steep edges to their intensity profile. The axonal EGFP signal was used to verify that each mitochondrion was inside the axon only after it was scored.

Data Analysis

A priori power calculations were performed in G*Power software (Faul et al., 2007) to calculate the number of newly-formed boutons required to detect a 10% difference in survival between the two mitochondrial conditions (less than or greater than 1.5 μm from a bouton). This calculation resulted in an estimated sample size of 450 newly-formed boutons. The number of animals required to achieve this was estimated from pilot studies to be 10–15 animals. In this study, 21 animals were used, 15 were imaged and 12 produced high-quality data that was included (see exclusion criteria below).

The final dataset was obtained from three different batches of littermates. A total of 51 ROIs and 306 axons were tracked. The total number of mitochondria counted across all time-points was 11,264 along with 4,892 unique boutons. Mitochondria were not linked between timepoints because they lacked individuality due to their ability to move, fuse and split (Lewis et al., 2018).

Some data were excluded from the final dataset. Any ROI that was too dim for accurate axon tracing (subjectively based on analyst experience) within the first four time points was not tracked. Any axon where the signal-to-noise in a session was low enough that the scorer could not be confident in bouton scoring was removed. Data from one animal that had only two axons tracked was also removed.

The bouton dynamic fraction was calculated as the proportion of unique boutons on an axon that were either lost or gained. Specifically, the sum of gains and losses divided by the total number of unique boutons across the two time-points: (gained + lost)/(gained + total$_{time1}$).

Mitochondrion and Bouton Co-localization

Mitochondria were classified as being present at a bouton if the distance between their centroids (defined by points placed by the analyst) was less than or equal to 1.5 μm. A dichotomous variable (mitochondria present or not) was chosen for analyses rather than a continuous variable (distance from nearest mitochondrion) because the axonal segment was a small sample of the axonal arbor and the true distance to the nearest mitochondria from each bouton could not be accurately measured, especially for boutons at the edge of the field of view. The distance of 1.5 μm was biologically-relevant because a distance-dependent relationship with synaptic ultrastructure has been seen up to 3 μm away (edge of vesicle pool to edge of mitochondrion) using electron microscopy (Smith et al., 2016). Stronger effects on synaptic ultrastructure were seen with closer distances of mitochondria. The accuracy of the measured distance in our study was limited due to the resolution of light microscopy and accuracy of point placement by the analyst, therefore only one distance was chosen in the middle of the range (0–3 μm).

The Randomization of bouton or mitochondrion position was carried out in a similar fashion to Smit-Rigter et al. (2016). Axons were first plotted in two dimensions in MATLAB using interpolation from segmented line coordinates recorded in ImageJ. The length of the axon was then estimated using Euclidean distances and a line was created and split into segments of 74 nm (the original pixel size of the 2P images). The real positions of the objects of interest (mitochondria or boutons) were plotted to the closest segment of the axon based on where they were in the original image using nearest neighbor distance calculations. Either mitochondria or boutons were then removed and randomly re-plotted along the axon without being placed closer than 1 μm together. Intervals of at least 1 μm were chosen to attempt to match the resolution limit with which two objects could be resolved using the 2P microscope in this study. This was repeated 1,000 times for each axon and the range plotted.

Statistics

Statistics were calculated using MATLAB (release 2016a), GraphPad Prism 7 or SPSS (IBM). Statistical significance was set at $p < 0.05$. Confidence intervals for proportions were calculated using the formula for single samples (Newcombe, 1998). The z^*-value for a 95% coverage of a gaussian distribution is 1.96. Therefore, the formula is as follows:

$$\hat{p} \pm z^* \sqrt{\frac{\hat{p}(1 - \hat{p})}{n}}$$

where prop1 is the proportion, z^* is 1.96 and N is the number of samples in the population. Errors are given as 95% confidence intervals for proportions and standard deviation for all other data, unless otherwise stated.

For repeated measures statistical tests, group sizes were matched by only including axons present in all relevant time-points for the particular test. To avoid pseudo-replication, samples were not pooled together across time from repeated measures.

A Gaussian mixture model was used to calculate posterior probabilities of axons being in EPB-rich or TB-rich groups based

on EPB and TB densities. An assumed number of two Gaussian components were defined by the analyst. Axons that fell under the threshold of 0.7 probability for both groups were not assigned a group.

Kaplan-Meier curves were created for survival analysis, based on time-to-event data. For bouton survival, this was the time from first observation until the bouton was no longer observed. Boutons that were no longer observed due to reasons other than loss were classed as 'censored' for the analysis.

RESULTS

To monitor presynaptic bouton structure alongside axonal mitochondria, we transduced neurons of the mouse primary and secondary motor cortex (M1 and M2) with an AAV that co-expressed cytosolic EGFP and mitochondrially-targeted (MTS)-TagRFP (**Figure 1A**). There was a substantial projection from the motor cortex made up of long-range axons that ramify in the ipsilateral somatosensory cortex (**Figure 1B**; Veinante and Deschênes, 2003; Petreanu et al., 2009; Mao et al., 2011; Oswald et al., 2013). Imaging of intact cleared brains showed that these axons travel over distances of more than 3 mm *via* cortical layers 5/6 or, to a lesser extent, superficially within layer 1 (**Supplementary Figures S1, S2**). By placing a cranial window over the primary somatosensory cortex (S1), we imaged segments of these long-range axons within layer 1 using *in vivo* 2P microscopy. Mitochondria, putative EPBs and *terminaux* boutons (TBs) were clearly identified as increases in fluorescence intensity along the local axon backbone (**Figure 1C**, see "Materials and Methods" section). We tracked structural synaptic plasticity of individual boutons by repeated imaging of the same axons at daily and weekly intervals over a total of up to 35 days (**Figure 1D**; $n = 12$ animals, 306 axons). Visual inspection (**Figure 1C**) and statistical analysis based on the density of EPBs and TBs along each axon (**Figure 1E**) indicated that axons were mostly either EPB-rich or TB-rich. As this is the first characterization of boutons in this axonal pathway, we compared the density and turnover of boutons in individual axonal branches. While there was a higher density of boutons in TB-rich axons, no differences were found in bouton turnover between EPB-rich and TB-rich axons (**Supplementary Figure S3**).

As mitochondria can support presynaptic function, we assessed whether the numerical density of boutons and mitochondria are correlated in axons (population mean overtime was 1.09 ± 0.41, 1 SD, and 0.69 ± 0.23 per 10 μm, respectively; **Figure 2A**). For individual axonal segments (median length of 75 μm, **Supplementary Figure S4**), there was a strong correlation between the densities of mitochondria and putative boutons (mean over time; Pearson's correlation, $R^2 = 0.50$, $p = 1.16 \times 10^{-20}$; **Figure 2B**). This suggested that the formation and/or elimination of boutons may relate to the mitochondrial population. To assess this, we compared the fraction of dynamic boutons (proportion lost *and* gained divided by the total number of unique boutons) across daily and weekly intervals to the mean mitochondrial density between the two time-points (**Figure 2C**, **Supplementary Table**

S1). Bouton dynamics were not significantly correlated to mitochondrial density in axonal segments at daily or weekly intervals ($R_s = 0.005$, Spearman's correlation, $p = 0.944$; **Figure 2C**, **Supplementary Table S1**). Similarly, there was no apparent correlation between bouton dynamics and mitochondrion-to-bouton ratios ($R_s = 0.024$, Spearman's correlation, $p = 0.733$; **Figure 2C**, **Supplementary Table S1**), indicating that the overall availability of mitochondria along a stretch of axon is not related to the degree of structural plasticity occurring there.

As the overall density of axonal mitochondria was related to bouton density, but not to bouton dynamics, we assessed if there was instead a more local relationship between individual boutons and mitochondria near them. Based on previous studies and effective resolution limits of our imaging, we chose 1.5 μm as a biologically relevant distance to presynaptic terminals Smith et al., 2016; Smit-Rigter et al., 2016; see "Materials and Methods" section). Whereas most mitochondria (65%) were found within 1.5 μm of presynaptic terminals (centroid-to-centroid distance; **Figure 3A**), only a minority of the total pool of putative boutons (44%) had mitochondria closer than 1.5 μm (**Figure 3B**). This local organization did not occur by chance, as randomizing or mirroring positions of either mitochondria or boutons along the axon backbone resulted in greater distances between them (**Figures 3A–C**). To determine if the structure of boutons affected the ability of mitochondria to localize there, we divided the bouton population into EPBs and TBs. There was a higher likelihood of mitochondria at EPBs ($45 \pm 3\%$, 95% CI) than TBs (measured from TB head, $27 \pm 3\%$; Chi-squared test, $p < 0.0001$; **Figures 3D–F**). It is possible that mitochondria reside near TBs, but do not traverse their neck region. Therefore, we estimated the location of the base of TBs by re-plotting them to where they joined the axon backbone (**Figure 3G**). The probability of mitochondria at the base of TBs was higher ($42 \pm 3\%$) than at the head, and not different from that of EPBs (data from day 0; Chi-squared test, $p = 0.188$; **Figures 3F,G**).

Given that mitochondria have been implicated in the control of presynaptic function, we hypothesized that mitochondrial presence may relate to bouton maturity. To test this hypothesis, we separated boutons by age (*new* or *pre-existing*; **Figure 4A**). New boutons were formed between daily imaging sessions (<24 h old), whereas pre-existing boutons were present before imaging began (mixed ages). Some pre-existing boutons would have been formed in the previous day and should have been classed as new boutons, but we estimated this to be <10% of the total population as this was the rate of daily bouton formation (**Supplementary Figure S5**). Pre-existing boutons were more likely than newly-formed boutons to have a resident mitochondrion (proportion with mitochondria on the first day tracked, *pre-existing* $38 \pm 2\%$, *new* $32 \pm 4\%$, 95% CI, Chi-squared test, $p = 0.0024$; **Figure 4B**). However, new boutons were still more likely to have mitochondria nearby than predicted by chance ($17 \pm 3\%$, 95% CI, Chi-squared test, $p < 0.0001$), as were pre-existing boutons ($17 \pm 2\%$, Chi-squared test, $p < 0.0001$; **Figure 4B**). Further to this, the likelihood of mitochondrial presence at long-lived boutons
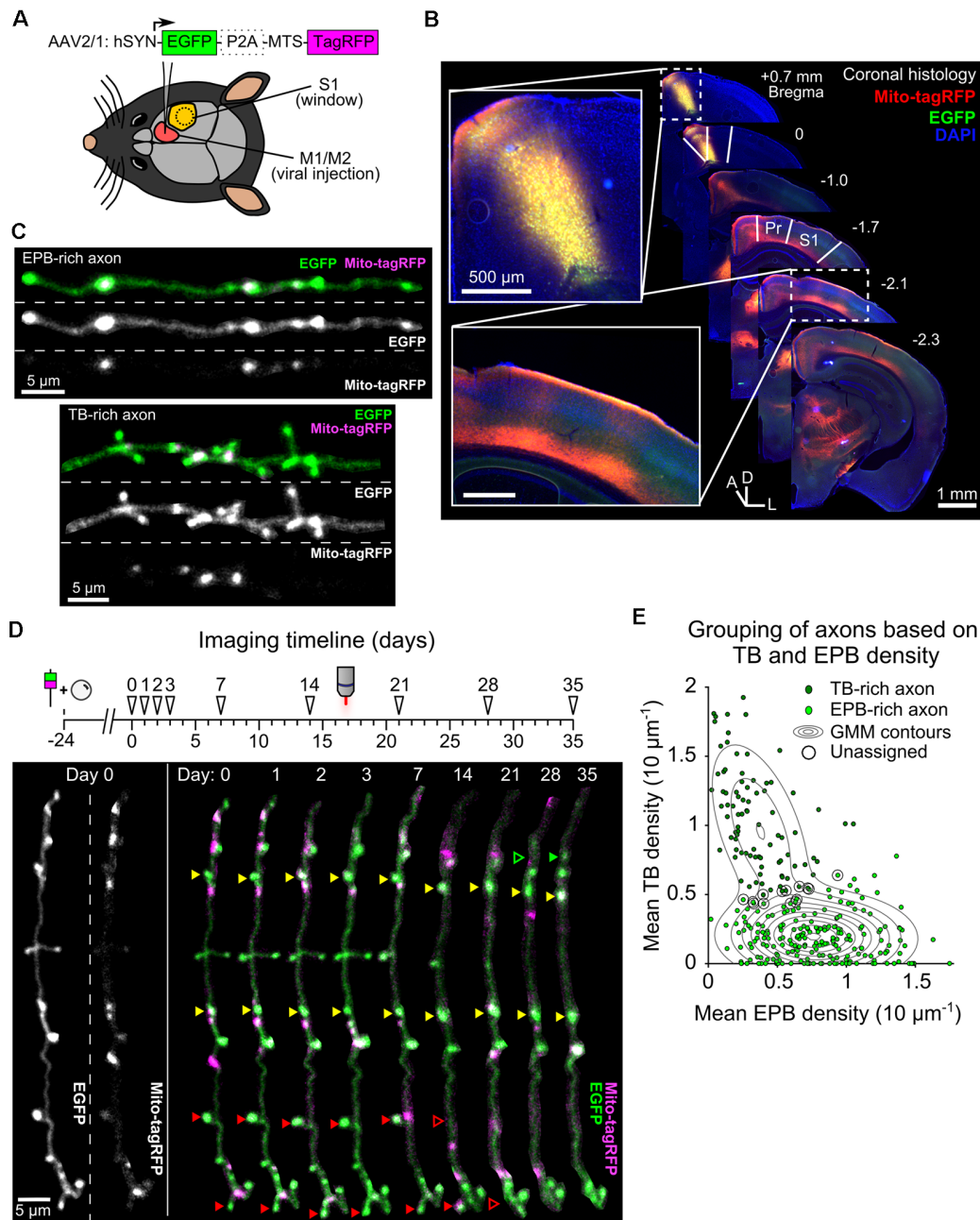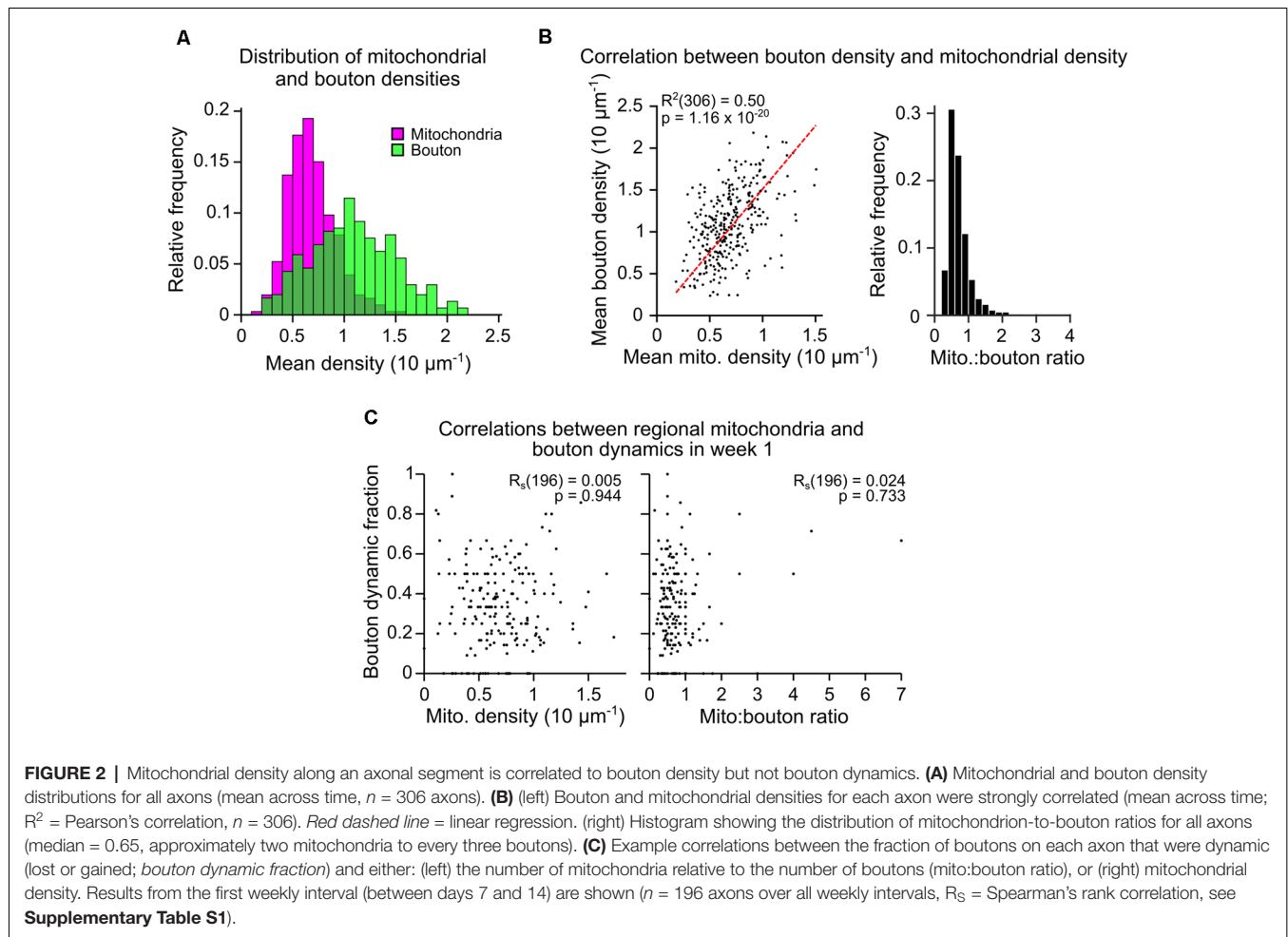
FIGURE 1 | Tracking bouton plasticity and mitochondrial positioning in axons of motor cortex neurons. **(A)** Adeno-associated virus (AAV) expressing cytosolic EGFP and a mitochondrial targeting sequence (MTS) conjugated to TagRFP was injected into M1/M2 and a glass cranial window was implanted over S1. **(B)** A series of coronal brain slices showing the viral injection site across the M1/M2 border (inset, top) and the axonal projection site at S1 under the cranial window (inset, bottom). Only the ipsilateral half of the brain sections are shown. Pr = parietal cortex, D = dorsal, L = lateral, A = anterior. **(C)** Cropped two-photon (2P) images from *in vivo* imaging show axons with high EPB density (EPB-rich) or high TB density (TB-rich). **(D)** (top) Imaging timeline for tracking bouton structural plasticity bouton loss and gain. Viral injection and cranial window implantation were performed 24 days prior to initial 2P imaging. Arrowheads indicate imaging time-points. (bottom) Structure and mitochondrial localization in a single cropped axon over 35 days imaged using *in vivo* 2P microscopy. Some boutons are labeled with arrowheads to show examples of stable (yellow), lost (red) or gained (green) boutons. **(E)** Gaussian mixture modeling (GMM) was used to determine two potential populations (*EPB-rich* and *TB-rich* axons) that result in the observed sample distribution of axonal EPB and TB densities (mean across time). Axons that had posterior probabilities below 70% were not assigned to a group (*circled*; see "Materials and Methods" section). Contour lines indicate the slope of the GMM distribution.

(those that survived the entire imaging period from the start) rose over time (*new* boutons 28 $\pm$ 12% to 43 $\pm$ 13%, *pre-existing* 46 $\pm$ 4% to 52 $\pm$ 4%, Cochran's Q test, *new*, $p = 0.235$,

pre-existing, $p < 0.0005$; **Figure 4C**). This was not the case with randomized mitochondrial positions, suggesting it is not a chance phenomenon (*pre-existing* 15 $\pm$ 3% to 18 $\pm$ 3%, *new*

FIGURE 2 | Mitochondrial density along an axonal segment is correlated to bouton density but not bouton dynamics. **(A)** Mitochondrial and bouton density distributions for all axons (mean across time, $n = 306$ axons). **(B)** (left) Bouton and mitochondrial densities for each axon were strongly correlated (mean across time; R^2 = Pearson's correlation, $n = 306$). *Red dashed line* = linear regression. (right) Histogram showing the distribution of mitochondrion-to-bouton ratios for all axons (median = 0.65, approximately two mitochondria to every three boutons). **(C)** Example correlations between the fraction of boutons on each axon that were dynamic (lost or gained; *bouton dynamic fraction*) and either: (left) the number of mitochondria relative to the number of boutons (mito:bouton ratio), or (right) mitochondrial density. Results from the first weekly interval (between days 7 and 14) are shown ($n = 196$ axons over all weekly intervals, R_S = Spearman's rank correlation, see **Supplementary Table S1**).

$13 \pm 9\%$ to $22 \pm 11\%$, Cochran's Q test, *new*, $p = 0.578$, *pre-existing*, $p = 0.134$). It was also not due to a general trend towards increased synaptic localization of mitochondria over time, as this was stable across the imaging paradigm (**Supplementary Figure S6**). These data show that the longer a bouton survives, the more likely it is to have a mitochondrion nearby.

It has been shown that newly-formed cortical boutons tend to be lost more quickly than pre-existing boutons (Qiao et al., 2015; Ash et al., 2018). Here, we show this is also true for boutons on long-range axons of motor cortical neurons, in which less than 30% of new boutons survived more than 1 week compared to ~70% survival for pre-existing boutons (median survival: *new*, 4 days, *pre-existing*, 35 days, Log-rank test, $p < 0.0001$; **Figure 4D**). Interestingly—despite their differing structures—TBs and EPBs show similar survival within these groups (**Figures 4E,F**), with only a small difference in median survival between new EPBs and TBs (*new EPB*, 4 days, *new TB*, 6 days, *pre-existing EPB* and *TB*, 35 days, Log-rank test, *new*, $p = 0.0006$, *pre-existing*, $p = 0.154$; **Figure 4F**). This aligns with the similarity in overall bouton turnover rates between EPB-rich and TB-rich axons (**Supplementary Figure S3**).

To determine if mitochondria relate to the stability of individual boutons locally, we assessed the survival of boutons with and without mitochondria. For new synaptic boutons, the chance of being removed was only slightly reduced if mitochondria were present (*without mitochondria* $45 \pm 6\%$ chance of being removed, *with mitochondria* $36 \pm 8\%$; Fisher's Exact test, $p = 0.031$; **Figure 4G**). As localization of mitochondria at TBs and EPBs appeared to be different, we assessed the impact of having resident mitochondria on the survival of the two bouton types separately. This stabilizing effect on new boutons appeared to be mediated by influence on EPBs, which were less likely to be lost if they had a mitochondrion, whereas we did not detect any mitochondrial influence on TB survival, albeit with lower n numbers (**Figure 4G**; Fisher's Exact test—EPBs, $p = 0.031$; TBs, $p = 0.784$). The effect was much more pronounced for older, pre-existing boutons, in which having mitochondria decreased the probability of subsequent removal by ~60% (*without mitochondria* $17 \pm 2\%$, *with mitochondria* $7 \pm 2\%$; Chi-squared, $p < 0.0005$; **Figure 4H**). This relationship between mitochondrial proximity and enhanced bouton survival was consistent across time for pre-existing boutons (**Supplementary Figure S7**). Again, we assessed whether the stabilization of boutons was dependent on bouton type. Even more strongly than in new boutons, mitochondrial presence was strongly
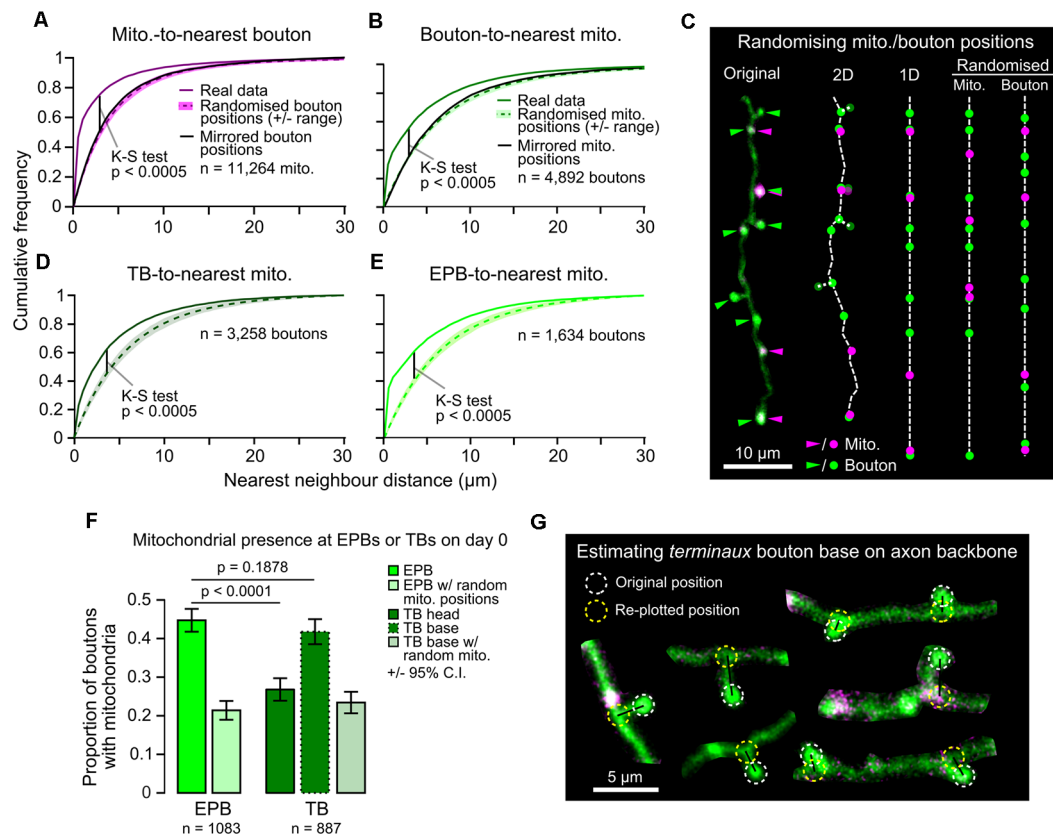
FIGURE 3 | Mitochondria are positioned more closely to *en passant* boutons (EPBs) than *terminaux* boutons (TBs). **(A)** The distribution of distances between each mitochondrion and its nearest bouton was plotted against the results from 1,000 rounds of randomized positioning of boutons for comparison to chance levels. Median ± range (*shaded area*). Kolmogorov–Smirnov (*K–S*) test between real data and the median of randomized positioning. As a further control, the real bouton positions were mirrored along the axon backbone to maintain the inter-bouton distances (*black line*) resulting in a similar distribution to the randomized positioning. **(B)** Same as in **(A)**, but for boutons and their nearest mitochondrion compared to results from randomized/mirrored positioning of mitochondria. **(C)** Illustration of the routine for randomizing positions. The original image was manually traced and a 2D skeleton interpolated from the segmented line trace. TBs were approximately placed at the nearest point on the axon backbone (their base) for randomizing in 1D. The 2D skeleton was then straightened to 1D and either mitochondria were randomly positioned alongside real bouton positions or vice versa. **(D,E)** Same as in **(B)**, but for TBs only (**D**; using TB base position, see **G**) or EPBs only **(E)**. **(F)** A greater proportion of EPBs have mitochondria within a biologically relevant distance (1.5 μm, see "Materials and Methods" section) than TBs (day 0 data; Chi-squared test). When mitochondrial localization was considered from the TB base instead of the head the difference was lost (Chi-squared test). Error bars ± 95% CI. **(G)** Estimated location of TB bases was achieved by finding the nearest neighbor point on the axon backbone that was closest to the TB head and re-plotting the TB to that position. 2P images were cropped for easier visualization.

related to decreased loss of pre-existing EPBs, but not of TBs (**Figure 4H**; Fisher's Exact test—EPBs, $p < 0.0005$; TBs, $p = 0.506$). Overall, these results suggest that the immediate survival of new boutons is weakly related to local mitochondrial presence, but this relationship becomes stronger and more consistent as boutons age.

DISCUSSION

It has long been reported that many, but not all, presynaptic release sites have mitochondria in close proximity to them (Gray, 1959; Shepherd and Harris, 1998; Chang et al., 2006; Kang et al., 2008; Obashi and Okabe, 2013; Smit-Rigter et al., 2016; Vaccaro et al., 2017). We found that axonal mitochondria in motor-somatosensory projection neurons are also preferentially associated with a subpopulation of synaptic boutons (**Figures 3**,

4B,C), suggesting bouton-specific recruitment and/or anchoring mechanisms (Kang et al., 2008; Courchet et al., 2013). The fact that mitochondria can modulate synaptic function suggests that having a resident mitochondrion may also relate to the activity-dependent plasticity of the synapse. Here, we have shown that there is indeed an association between mitochondrial positioning at presynaptic terminals and their structural longevity. As with other axons (De Paola et al., 2006; Qiao et al., 2015; Ash et al., 2018; Morimoto et al., 2018), we found that these motor-somatosensory axons exhibit structural plasticity driven by the turnover of a minority of their synaptic boutons (**Figures 4D–F**). Newly-formed boutons are more likely to possess mitochondria within their first 24 h (our smallest imaging interval) than by chance (**Figure 4B**), suggesting a link between synaptic and mitochondrial function even in the early stages of the synaptic lifecycle. Long-lasting
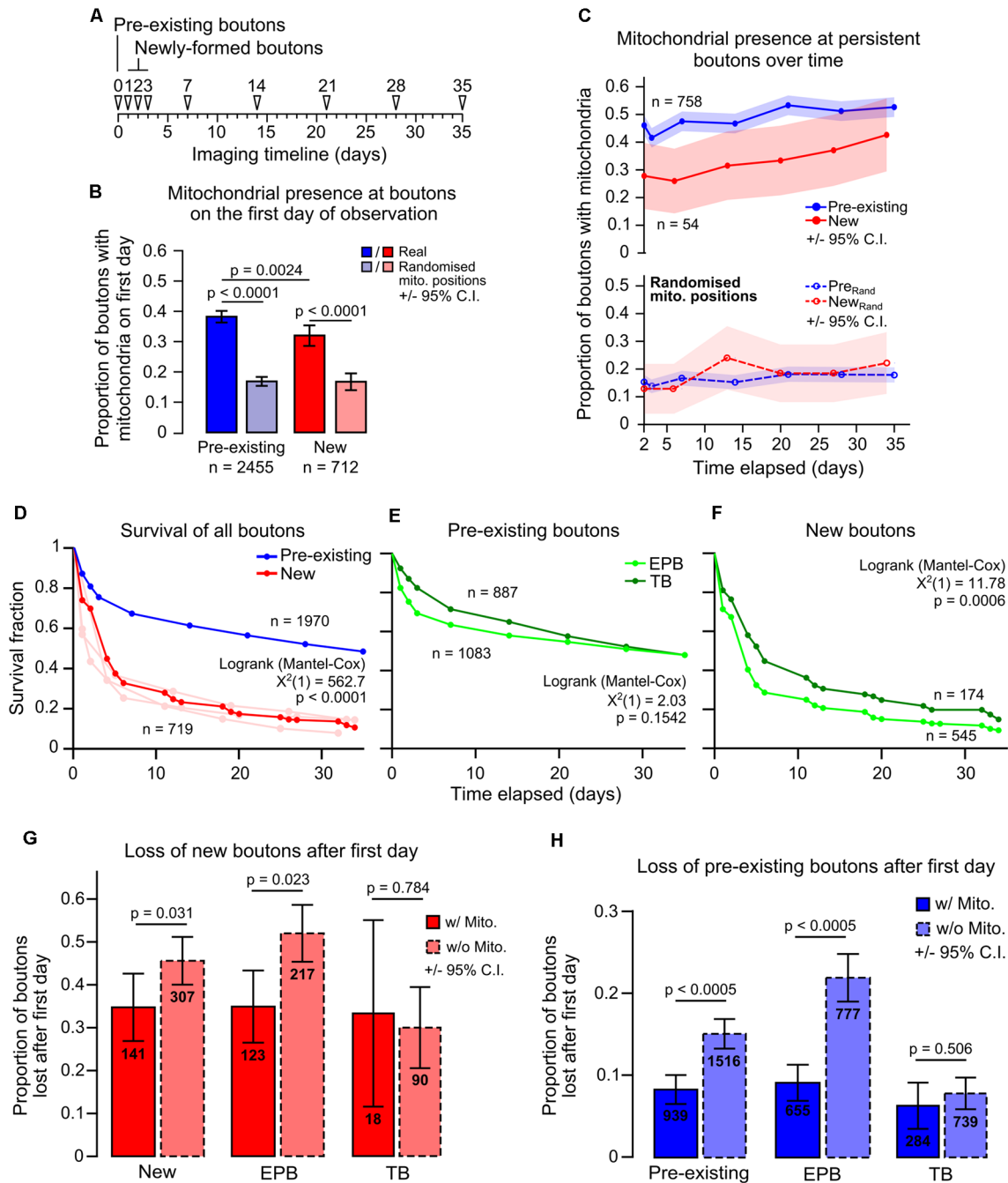
FIGURE 4 | Mitochondrial presence at individual boutons is positively related to bouton age and longevity. (**A**) Timeline indicating the classification of pre-existing boutons (first identified on day 0) and newly-formed boutons (first identified on days 1, 2 or 3). (**B**) Pre-existing boutons were more likely to have mitochondria (<1.5 μm) than newly-formed boutons (Chi-squared test). Newly-formed boutons had more mitochondria present than with randomized positioning of mitochondria, as did pre-existing boutons (Chi-squared test). Error bars ± 95% CI. (**C**) Boutons that persisted in every time point after day 2 (after all newly-formed boutons were identified) had their mitochondrial localization tracked. Pre-existing boutons showed a significant increase in mitochondrial presence (Cochran's Q test: $\chi^2_{(6)} = 51.359$, $p < 0.0005$). New boutons also showed an increase; however, this was not statistically significant (Cochran's Q test: $\chi^2_{(5)} = 6.81$, $p = 0.235$). When mitochondrial positions were randomized, both new and pre-existing boutons did not show significant increases in mitochondrial localization (Cochran's Q test: New, $\chi^2_{(5)} = 3.807$, $p = 0.578$; pre-existing, $\chi^2_{(6)} = 9.787$, $p = 0.134$). Shaded areas are ± 95% CI. (**D**) Survival of boutons was measured as the time until bouton loss. Pre-existing boutons were significantly more stable than new boutons (Log-rank test). The new bouton population was pooled from day 1–3 (light red lines). (**E,F**) Of the pre-existing population, TB and EPB survival was similar (**E**), however, there was a small significant decrease in survival for new EPBs compared to TBs (**F**; Log-rank test). (**G**) The proportion of new boutons with or without mitochondria that were lost after their first day. There was a significant decrease in bouton loss when mitochondria were present at new boutons (Fisher's exact test). This relationship was due to the population of EPBs and not TBs. (**H**) Similarly, pre-existing EPBs with mitochondria were half as likely to be lost when compared to those without mitochondria (Fisher's exact test). Error bars ± 95% CI.

boutons are even more likely to have resident mitochondria (**Figures 4B,C**) and this decreases the chance of those boutons being removed by half (**Figure 4H**). This results in a persisting population of synaptic boutons that are more likely to contain mitochondria. As such, it seems likely that mitochondrial recruitment links to some synaptic function that promotes synaptic longevity (Rangaraju et al., 2019). This aligns with the previous finding that, in local axons within the visual cortex, boutons without mitochondria are more likely to be lost over a 4-day period (Smit-Rigter et al., 2016). Presynaptic mitochondria can modulate short-term plasticity of neurotransmitter release *via* their sequestration and slow release of calcium (Billups and Forsythe, 2002; Sun et al., 2013; Kwon et al., 2016). Also, presynaptic release probability does correlate with overall synaptic strength and vesicle pool size suggesting that there may be a link between mitochondrial influence on presynaptic release and the likelihood of a synapse becoming stronger and/or more stable (Monday et al., 2018). However, it remains unknown whether mitochondria directly influence long-term plasticity of synaptic function, as recently shown within dendrites (Smith et al., 2016; Divakaruni et al., 2018), or are simply recruited by alterations in synaptic activity to support ongoing presynaptic function (Vaccaro et al., 2017).

Our data suggest that any link between mitochondria and plasticity is local to neighboring synapses. This is because, although the density of mitochondria along different axonal branches varied considerably, it did not correlate with rates of bouton plasticity at the branch level (**Figure 2**). In contrast, the close proximity of mitochondria (within 1.5 μm) did relate to individual bouton stability (**Figure 4**). Mitochondria can be highly dynamic, undergoing rapid rounds of fusion and fission alongside axonal trafficking (Lewis et al., 2018), making it difficult to identify individual mitochondria over long periods of time with low imaging frequency. However, it has been reported that, despite the overall axonal positioning of mitochondria being unstable, there are more likely to be mitochondria stably retained near boutons than non-synaptic locations (Smit-Rigter et al., 2016). In this study, we found that the spatial arrangement of mitochondria and synaptic boutons depends on bouton type as mitochondria were generally located closer to EPBs than to TBs (**Figure 3**). This may be because physical access to the bouton head is restricted by the neck of TBs or could reflect functional differences between bouton types. Indeed, the difference in proximity was mirrored by the fact that local mitochondria were strongly linked to the survival of EPBs but not TBs. Interestingly, reported alterations in the stability of EPBs associated with aging might hint at parallel changes in synapse-mitochondrial coupling in the aged brain (Grillo et al., 2013). There is no information on potentially different mechanisms linking mitochondria to presynaptic function or plasticity in TBs vs. EPBs. Perhaps the longer distance between active zone and mitochondria in TB alters the way in which mitochondria can influence local signals, such as Ca^{2+}, that may be crucial for plasticity. Potentially divergent plasticity mechanisms at TBs and EPBs highlights the need for further investigation of the underexplored differences between different axonal bouton types.

DATA AVAILABILITY STATEMENT

The datasets generated for this study are available on request to the corresponding author.

ETHICS STATEMENT

All studies involving animals adhered to the Animals (Scientific Procedures) Act 1986 and Amendment Regulations 2012 as outlined in UK law and approved by the University of Bristol Animal Welfare and Ethics Review Board.

AUTHOR CONTRIBUTIONS

RL, JJ, and MA designed, developed and carried out the experiments and analysis. RL and MA wrote the manuscript.

FUNDING

ACKNOWLEDGMENTS

We thank the Wolfson Bioimaging Facility for their support and expertise and MRC funding of a preclinical *in vivo* functional imaging platform for translational regenerative medicine. We thank Lilly UK for the gift of the AAV used in this study. This manuscript has been released as a preprint in BioRxiv (Lees et al., 2019).

SUPPLEMENTARY MATERIAL

The Supplementary Material for this article can be found online at: https://www.frontiersin.org/articles/10.3389/fnsyn. 2019.00037/full#supplementary-material.

REFERENCES

Ash, R. T., Fahey, P. G., Park, J., Zoghbi, H. Y., and Smirnakis, S. M. (2018). Increased axonal bouton stability during learning in the mouse model of MECP2 duplication syndrome. *eNeuro* 5:ENEURO.0056-17.2018. doi: 10.1523/eneuro.0056-17.2018

Billups, B., and Forsythe, I. D. (2002). Presynaptic mitochondrial calcium sequestration influences transmission at mammalian central synapses. *J. Neurosci.* 22, 5840–5847.

Briones, T. L., Klintsova, A. Y., and Greenough, W. T. (2004). Stability of synaptic plasticity in the adult rat visual cortex induced by complex environment exposure. *Brain Res.* 1018, 130–135. doi: 10.1016/j.brainres.2004.06.001

Chang, D. T. W., Honick, A. S., and Reynolds, I. J. (2006). Mitochondrial trafficking to synapses in cultured primary cortical neurons. *J. Neurosci.* 26, 7035–7045. doi: 10.1523/jneurosci.1012-06.2006

Courchet, J., Lewis, T. L., Lee, S., Courchet, V., Liou, D.-Y., Aizawa, S., et al. (2013). Terminal axon branching is regulated by the LKB1-NUAK1 kinase pathway *via* presynaptic mitochondrial capture. *Cell* 153, 1510–1525. doi: 10.1016/j.cell.2013.05.021

Cserép, C., Pósfai, B., Schwarcz, A. D., and Dénes, Á. (2018). Mitochondrial ultrastructure is coupled to synaptic performance at axonal release sites. *eNeuro* 5:ENEURO.0390-17.2018. doi: 10.1523/eneuro.0390-17.2018

De Paola, V., Holtmaat, A., Knott, G., Song, S., Wilbrecht, L., Caroni, P., et al. (2006). Cell type-specific structural plasticity of axonal branches and boutons in the adult neocortex. *Neuron* 49, 861–875. doi: 10.1016/j.neuron.2006.02.017

Divakaruni, S. S., Dyke, A. M. V., Chandra, R., LeGates, T. A., Contreras, M., Dharmasri, P. A., et al. (2018). Long-term potentiation requires a rapid burst of dendritic mitochondrial fission during induction. *Neuron* 100, 860.e7–875.e7. doi: 10.1016/j.neuron.2018.09.025

Edelstein, A. D., Tsuchida, M. A., Amodaj, N., Pinkard, H., Vale, R. D., and Stuurman, N. (2014). Advanced methods of microscope control using μManager software. *J. Biol. Methods* 1:e10. doi: 10.14440/jbm.2014.36

Faul, F., Erdfelder, E., Lang, A.-G., and Buchner, A. (2007). G*Power 3: a flexible statistical power analysis program for the social, behavioral and biomedical sciences. *Behav. Res. Methods* 39, 175–191. doi: 10.3758/bf03193146

Franklin, K., and Paxinos, G. (2008). *The Mouse Brain in Stereotaxic Coordinates.* San Diego, CA: Academic Press.

Gray, E. G. (1959). Axo-somatic and axo-dendritic synapses of the cerebral cortex: an electron microscope study. *J. Anat.* 93, 420–433.

Grillo, F. W., Song, S., Teles-Grilo Ruivo, L. M., Huang, L., Gao, G., Knott, G. W., et al. (2013). Increased axonal bouton dynamics in the aging mouse cortex. *Proc. Natl. Acad. Sci. U S A* 110, E1514–E1523. doi: 10.1073/pnas.1218731110

Hall, C. N., Klein-Flügge, M. C., Howarth, C., and Attwell, D. (2012). Oxidative phosphorylation, not glycolysis, powers pre- and postsynaptic mechanisms underlying brain information processing. *J. Neurosci.* 32, 8940–8951. doi: 10.1523/jneurosci.0026-12.2012

Holtmaat, A., and Caroni, P. (2016). Functional and structural underpinnings of neuronal assembly formation in learning. *Nat. Neurosci.* 19, 1553–1562. doi: 10.1038/nn.4418

Holtmaat, A., Bonhoeffer, T., Chow, D. K., Chuckowree, J., Paola, V. D., Hofer, S. B., et al. (2009). Long-term, high-resolution imaging in the mouse neocortex through a chronic cranial window. *Nat. Protoc.* 4, 1128–1144. doi: 10.1038/nprot.2009.89

Jackson, J. S., Witton, J., Johnson, J. D., Ahmed, Z., Ward, M., Randall, A. D., et al. (2017). Altered synapse stability in the early stages of tauopathy. *Cell Rep.* 18, 3063–3068. doi: 10.1016/j.celrep.2017.03.013

Johnson, C. M., Peckler, H., Tai, L.-H., and Wilbrecht, L. (2016). Rule learning enhances structural plasticity of long-range axons in frontal cortex. *Nat. Commun.* 7:10785. doi: 10.1038/ncomms10785

Kang, J.-S., Tian, J.-H., Pan, P.-Y., Zald, P., Li, C., Deng, C., et al. (2008). Docking of axonal mitochondria by syntaphilin controls their mobility and affects short-term facilitation. *Cell* 132, 137–148. doi: 10.1016/j.cell.2007.11.024

Kasthuri, N., Hayworth, K. J., Berger, D. R., Schalek, R. L., Conchello, J. A., Knowles-Barley, S., et al. (2015). Saturated reconstruction of a volume of neocortex. *Cell* 162, 648–661. doi: 10.1016/j.cell.2015.06.054

Kim, J. H., Lee, S.-R., Li, L.-H., Park, H.-J., Park, J.-H., Lee, K. Y., et al. (2011). High cleavage efficiency of a 2A peptide derived from porcine teschovirus-1 in human cell lines, zebrafish and mice. *PLoS One* 6:e18556. doi: 10.1371/journal.pone.0018556

Kwon, S.-K., Iii, R. S., Lewis, T. L., Hirabayashi, Y., Maximov, A., and Polleux, F. (2016). LKB1 regulates mitochondria-dependent presynaptic calcium clearance and neurotransmitter release properties at excitatory synapses along cortical axons. *PLoS Biol.* 14:e1002516. doi: 10.1371/journal.pbio.1002516

Landers, M. S., Knott, G. W., Lipp, H. P., Poletaeva, I., and Welker, E. (2011). Synapse formation in adult barrel cortex following naturalistic environmental enrichment. *Neuroscience* 199, 143–152. doi: 10.1016/j.neuroscience.2011.10.040

Lee, E., Choi, J., Jo, Y., Kim, J. Y., Jang, Y. J., Lee, H. M., et al. (2016). ACT-PRESTO: rapid and consistent tissue clearing and labeling method for 3-dimensional (3D) imaging. *Sci. Rep.* 6:18631. doi: 10.1038/srep18631

Lees, R. M., Johnson, J. D., and Ashby, M. C. (2019). Presynaptic boutons that contain mitochondria are more stable. *BioRxiv [Preprint].* doi: 10.1101/580530

Lein, E. S., Hawrylycz, M. J., Ao, N., Ayres, M., Bensinger, A., Bernard, A., et al. (2007). Genome-wide atlas of gene expression in the adult mouse brain. *Nature* 445, 168–176. doi: 10.1038/nature05453

Lewis, T. L., Kwon, S.-K., Lee, A., Shaw, R., and Polleux, F. (2018). MFF-dependent mitochondrial fission regulates presynaptic release and axon branching by limiting axonal mitochondria size. *Nat. Commun.* 9:5008. doi: 10.1038/s41467-018-07416-2

Mao, T., Kusefoglu, D., Hooks, B. M., Huber, D., Petreanu, L., and Svoboda, K. (2011). Long-range neuronal circuits underlying the interaction between sensory and motor cortex. *Neuron* 72, 111–123. doi: 10.1016/j.neuron.2011.07.029

Monday, H. R., Younts, T. J., and Castillo, P. E. (2018). Long-term plasticity of neurotransmitter release: emerging mechanisms and contributions to brain function and disease. *Ann. Rev. Neurosci.* 41, 299–322. doi: 10.1146/annurev-neuro-080317-062155

Morimoto, M. M., Tanaka, S., Mizutani, S., Urata, S., Kobayashi, K., and Okabe, S. (2018). *In vivo* observation of structural changes in neocortical catecholaminergic projections in response to drugs of abuse. *eNeuro* 5:ENEURO.0071-17.2018. doi: 10.1523/eneuro.0071-17.2018

Mostany, R., Anstey, J. E., Crump, K. L., Maco, B., Knott, G., and Portera-Cailliau, C. (2013). Altered synaptic dynamics during normal brain aging. *J. Neurosci.* 33, 4094–4104. doi: 10.1523/JNEUROSCI.4825-12.2013

Newcombe, R. G. (1998). Two-sided confidence intervals for the single proportion: comparison of seven methods. *Stat. Med.* 17, 857–872. doi: 10.1002/(sici)1097-0258(19980430)17:8<857::aid-sim777>3.0.co;2-e

Nithianantharajah, J., Levis, H., and Murphy, M. (2004). Environmental enrichment results in cortical and subcortical changes in levels of synaptophysin and PSD-95 proteins. *Neurobiol. Learn. Mem.* 81, 200–210. doi: 10.1016/j.nlm.2004.02.002

Obashi, K., and Okabe, S. (2013). Regulation of mitochondrial dynamics and distribution by synapse position and neuronal activity in the axon. *Eur. J. Neurosci.* 38, 2350–2363. doi: 10.1111/ejn.12263

Oswald, M. J., Tantirigama, M. L. S., Sonntag, I., Hughes, S. M., and Empson, R. M. (2013). Diversity of layer 5 projection neurons in the mouse motor cortex. *Front. Cell. Neurosci.* 7:174. doi: 10.3389/fncel.2013.00174

Petreanu, L., Gutnisky, D. A., Huber, D., Xu, N., O'Connor, D. H., Tian, L., et al. (2012). Activity in motor-sensory projections reveals distributed coding in somatosensation. *Nature* 489, 299–303. doi: 10.1038/nature11321

Petreanu, L., Mao, T., Sternson, S. M., and Svoboda, K. (2009). The subcellular organization of neocortical excitatory connections. *Nature* 457, 1142–1145. doi: 10.1038/nature07709

Pologruto, T. A., Sabatini, B. L., and Svoboda, K. (2003). ScanImage: flexible software for operating laser scanning microscopes. *Biomed. Eng. Online* 2:13. doi: 10.1186/1475-925X-2-13

Qiao, Q., Ma, L., Li, W., Tsai, J.-W., Yang, G., and Gan, W.-B. (2015). Long-term stability of axonal boutons in the mouse barrel cortex. *Dev. Neurobiol.* 76, 252–261. doi: 10.1002/dneu.22311

Rangaraju, V., Calloway, N., and Ryan, T. A. (2014). Activity-driven local ATP synthesis is required for synaptic function. *Cell* 156, 825–835. doi: 10.1016/j.cell.2013.12.042

Rangaraju, V., Lauterbach, M., and Schuman, E. M. (2019). Spatially stable mitochondrial compartments fuel local translation during plasticity. *Cell* 176, 73.e15–84.e15. doi: 10.1016/j.cell.2018.12.013

Schindelin, J., Arganda-Carreras, I., Frise, E., Kaynig, V., Longair, M., Pietzsch, T., et al. (2012). Fiji: an open-source platform for biological-image analysis. *Nat. Methods* 9, 676–682. doi: 10.1038/nmeth.2019

Shepherd, G. M. G., and Harris, K. M. (1998). Three-dimensional structure and composition of CA3→CA1 axons in rat hippocampal slices: implications for presynaptic connectivity and compartmentalization. *J. Neurosci.* 18, 8300–8310. doi: 10.1523/jneurosci.18-20-08300.1998

Smith, H. L., Bourne, J. N., Cao, G., Chirillo, M. A., Ostroff, L. E., Watson, D. J., et al. (2016). Mitochondrial support of persistent presynaptic vesicle mobilization with age-dependent synaptic growth after LTP. *Elife* 5:e15275. doi: 10.7554/eLife.15275

Smit-Rigter, L., Rajendran, R., Silva, C. A. P., Spierenburg, L., Groeneweg, F., Ruimschotel, E. M., et al. (2016). Mitochondrial dynamics in visual cortex are limited *in vivo* and not affected by axonal structural plasticity. *Curr. Biol.* 26, 2609–2616. doi: 10.1016/j.cub.2016.07.033

Sobieski, C., Fitzpatrick, M. J., and Mennerick, S. J. (2017). Differential presynaptic ATP supply for basal and high-demand transmission. *J. Neurosci.* 37, 1888–1899. doi: 10.1523/jneurosci.2712-16.2017

Song, S., Grillo, F. W., Xi, J., Ferretti, V., Gao, G., and De Paola, V. (2016). EPBscore: a novel method for computer-assisted analysis of axonal structure and dynamics. *Neuroinformatics* 14, 121–127. doi: 10.1007/s12021-015-9274-5

Sun, T., Qiao, H., Pan, P.-Y., Chen, Y., and Sheng, Z.-H. (2013). Motile axonal mitochondria contribute to the variability of presynaptic strength. *Cell Rep.* 4, 413–419. doi: 10.1016/j.celrep.2013.06.040

Vaccaro, V., Devine, M. J., Higgs, N. F., and Kittler, J. T. (2017). Miro1-dependent mitochondrial positioning drives the rescaling of presynaptic Ca^{2+} signals during homeostatic plasticity. *EMBO Rep.* 18, 231–240. doi: 10.15252/embr.201642710

Veinante, P., and Deschênes, M. (2003). Single-cell study of motor cortex projections to the barrel field in rats. *J. Comp. Neurol.* 464, 98–103. doi: 10.1002/cne.10769

Zufferey, R., Donello, J. E., Trono, D., and Hope, T. J. (1999). Woodchuck hepatitis virus posttranscriptional regulatory element enhances expression of transgenes delivered by retroviral vectors. *J. Virol.* 73, 2886–2892.